DRYLANDS

Dryland self-expansion enabled by land–atmosphere feedbacks

Akash Koppa[1,2]*, Jessica Keune[1,3], Dominik L. Schumacher[4], Katerina Michaelides[5,6], Michael Singer[6,7], Sonia I. Seneviratne[4], Diego G. Miralles[1]

Dryland expansion causes widespread water scarcity and biodiversity loss. Although the drying influence of global warming is well established, the role of existing drylands in their own expansion is relatively unknown. In this work, by tracking the air flowing over drylands, we show that the warming and drying of that air contributes to dryland expansion in the downwind direction. As they dry, drylands contribute less moisture and more heat to downwind humid regions, reducing precipitation and increasing atmospheric water demand, which ultimately causes their aridification. In ~40% of the land area that recently transitioned from a humid region into a dryland, self-expansion accounted for >50% of the observed aridification. Our results corroborate the urgent need for climate change mitigation measures in drylands to decelerate their own expansion.

Drylands are often defined as regions in which the atmospheric water demand [potential evaporation (E_p)] substantially exceeds supply [precipitation (P)] (*1*, *2*). Currently, they occupy ~45% of Earth's land surface (*3*) and have been highlighted as hotspots of climate change (*4*–*6*), yet how the global distribution of drylands will evolve under a changing climate remains unclear. From an atmospheric aridity perspective (often represented by the aridity index: AI = E_p/P), there is strong evidence of intensified aridification of existing drylands and their expansion into more humid regions (*7*–*9*). Debates persist around whether an atmosphere-centric metric of aridity such as AI is appropriate for identifying drylands and quantifying their expansion because actual evaporation in drylands may not increase owing to soil moisture limitation (*10*, *11*) and the influence of CO_2 fertilization on vegetation and water use efficiency (*12*, *13*). Nonetheless, the degree to which increasing water use efficiency can counteract the effects of atmospheric aridity on vegetation remains uncertain (*14*, *15*), particularly in dry conditions (*16*, *17*). Moreover, field experiments, observations, and model-based studies have established unequivocal links between atmospheric aridity and adverse changes in water availability (*18*–*20*), ecosystem function (*21*), stability of soils (*9*), and nutrient cycling (*22*); a comprehensive overview of the advantages of an atmospheric definition of aridity for this study is presented in the supplementary materials (*23*). Therefore, it is vital to improve our understanding of the processes that drive increases in atmospheric aridity over humid regions and ultimately cause dryland expansion.

From an atmospheric perspective, dryland expansion is assumed to take place when AI surpasses a threshold of 1.55, which represents a shift from the humid to the dry subhumid class as defined by the World Atlas of Desertification (*24*). This shift occurs when P becomes lower than 65% of E_p or E_p becomes larger than P by >55% for a prolonged period (a minimum of 10 years in this study). Changes in E_p are inextricably linked to increasing temperature under rising greenhouse gases and associated changes in relative humidity and vapor pressure deficit (*25*, *26*). E_p has exhibited significant positive trends in historical records (*27*) and is projected to further increase in the future (*28*, *29*), thus driving ecosystems into a more arid regime worldwide (*30*, *31*). Although E_p increases are largely consistent with temperature trends, changes in P and their potential drivers are more complex. In the long term, global warming can alter the atmospheric water-holding capacity, its stability, and large-scale circulation patterns (*32*, *33*), resulting in systematic changes in the spatiotemporal patterns of P. Because of these complex changes, simple paradigms such as "dry gets drier and wet gets wetter" are unable to accurately explain the observed trends in P over land, especially in transitional regimes on the edge between drylands and humid regions (*11*, *34*).

At subseasonal to seasonal timescales, the causes of P deficits are better understood; anomalous anticyclonic conditions created by shifts in global circulation patterns, often associated with anomalies in sea surface temperatures, can cause deficits in P, which can potentially evolve into a drought (*35*, *36*). Then, the land dry-out can reinforce both P deficits and E_p increases through what is typically referred to as positive land–atmosphere feedbacks (*37*, *38*): Deficits in P lead to drier soil and vegetation, which often result in a decreased air moistening [through evaporation (E)] and increased warming [through sensible heat flux (H)], which in turn reduces precipitable water and increases E_p (*37*). Moreover, these land feedbacks can influence the atmosphere of downwind regions through advection of (i) drier air, which leads to a reduction in the total moisture available for P (*39*), and (ii) warmer air, which leads to an increase in air temperature (*40*) and consequently E_p (*41*, *42*). However, the degree to which the downwind propagation of P deficits and E_p increases caused by land–atmosphere feedbacks in upwind drylands can contribute to the aridification of downwind humid environments (expansion of drylands) over the multiannual timescales at which aridification occurs remains unknown.

We investigated the role of drylands in the aridification of downwind humid regions over multiple decades and across the global land surface. We hypothesized that drylands contribute to their own expansion through land–atmosphere feedbacks, which leads to the aridification of downwind humid regions, a process we term "dryland self-expansion." We quantified the importance of this process by spatiotemporally tracking the atmospheric moisture and heat transported into humid–dry transitioning regions using 38 years (1981 to 2018) of simulations from an observationally constrained Lagrangian atmospheric transport model (*23*). Reductions in moisture transported through drier air can affect P (eq. S5), and increased heat transport through warmer air can affect E_p (eqs. S6 and S7) through changes in air temperature and vapor pressure deficit. Therefore, by using the Lagrangian model, we can trace the origins of both the observed P deficits and E_p increases that drive the aridification of downwind humid regions and isolate the relevance of upwind drylands. In addition, we quantified the changes in the land surface fluxes within upwind drylands that initiate and promote their self-expansion.

Global dryland expansion

Between 1981 and 2018, ~5.2 million km^2 of humid land transitioned into a dryland (table S1). By accounting for dryland contraction (~1.3 million km^2), this represents a ~9% expansion in global dryland area. Long-term expansion into humid regions is observed in all major drylands across the globe, with Eurasia witnessing the largest, followed by Africa and South America (Fig. 1 and table S1). The extent of dryland expansion is robust and

[1]Hydro-Climate Extremes Lab (H-CEL), Ghent University, Ghent, Belgium. [2]Laboratory of Catchment Hydrology and Geomorphology, École Polytechnique Fédérale de Lausanne, Sion, Switzerland. [3]European Centre for Medium-Range Weather Forecasts, Bonn, Germany. [4]Department of Environmental Systems Science, Institute for Atmospheric and Climate Science, ETH Zurich, Zurich, Switzerland. [5]School of Geographical Sciences, University of Bristol, Bristol, UK. [6]Earth Research Institute, University of California Santa Barbara, Santa Barbara, CA, USA. [7]School of Earth and Environmental Sciences, Cardiff University, Cardiff, UK.
*Corresponding author. Email: akash.koppa@ugent.be

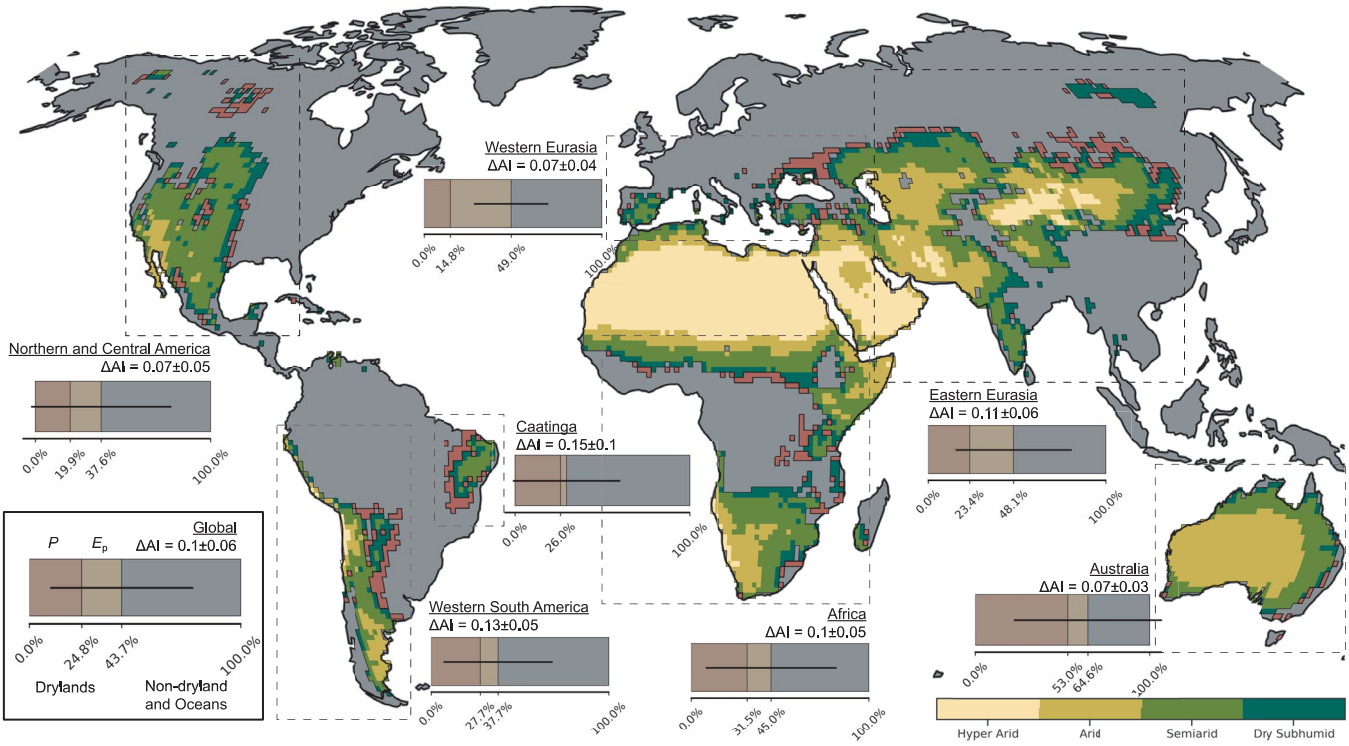

Fig. 1. Global prevalence of dryland self-expansion. Global map of existing (shades of green) and expanding (red) drylands. The stacked bar plots show the degree to which the increase in aridity index (ΔAI) over the expanded drylands can be attributed to reduced *P* (brown) and increased E_p (tan) from existing drylands (self-expansion) and other regions, including upwind oceans and humid regions (gray), across the globe. The black bar indicates the spread (1 SD) in the combined importance of self-expansion across all the expanding drylands. The extent of the upwind drylands corresponds to the year 1980, which represents the initial state in our analysis. The expanding dryland regions are estimated over the subsequent period 1981 to 2018 (*23*). The dashed boxes encompass regions that have transitioned from a humid region to a dryland during the study period. AI is defined here as E_p/P, which is consistent with several previous studies (*21*, *54*, *55*). An alternative version of the figure with AI defined as P/E_p is presented in the supplementary materials (fig. S5).

independent of the resolution of the input datasets (fig. S2), the specific choice of *P* and E_p datasets (fig. S3), and the exact threshold of AI used to define drylands (fig. S4). In relative terms, the Caatinga drylands have expanded the most (79%), followed by the South American drylands (26%) (table S1). These patterns are consistent with recent studies that have documented drying trends in the southwest of the United States of America (*43*), Congo (*44*), central Asia (*45*), and the Caatinga (*46*). However, the largest dryland contraction of ~0.5 million km^2 is observed in North America, primarily in the Midwest, and eastern Eurasia (fig. S1 and table S1). Dryland expansion and contraction is concentrated in regions bordering existing drylands, as expected. Likewise, there is a large variance in the degree of aridification, with the largest AI increases of up to 60% being in the Caatinga (fig. S6).

Decomposing the increase in atmospheric aridity into its first-order drivers (*P* and E_p) (*23*), we found that globally, the relative contribution of changes in *P* (mean and spread of 54.9 ± 26%) is larger than that of E_p (45.1 ± 26%). However, the relative importance of *P* and E_p expresses high spatial variability across the globe (Fig. 2); although decreases in *P* play a more important role in South America and Africa, increases in E_p explain most of the aridification in the western parts of Eurasia (figs. S3 and S4). These spatial patterns are primarily driven by *P* changes, which show much higher variance than those in E_p. Nevertheless, several regions underwent a humid–dry transition despite experiencing small increases in *P*, which were thus counteracted by disproportionate increases in E_p (Fig. 2, Q1 and Q2) (*47*).

Contribution of dryland self-expansion

Using a Lagrangian atmospheric model constrained by reanalysis and observation-based estimates of *P* and *E* (*23*, *48*), we quantified the contribution of existing drylands to their own expansion. Globally, in ~40% of the ~5.2 million km^2 of humid land area transitioning into dryland, self-expansion accounts for >50% of the increase in aridity. In parts of Australia and Eurasia, self-expansion is the dominant mechanism by which drylands spread (fig. S12), accounting for >50% of the aridity increase. We also found strong intraregional variability in the importance of self-expansion, especially in Africa, the Caatinga, and the eastern parts of Eurasia (fig. S12). Although the drying of the Congo bordering the East Sudanian savanna is primarily driven by self-expansion, this mechanism plays a smaller role in the expansion of the East African drylands. Similarly, we observed an increasing importance of self-expansion from north to south in the Caatinga and from east to west in eastern Eurasia (fig. S12). Furthermore, we found that more than half of the global self-expansion is due to the reduction in *P* contribution from upwind drylands (Fig. 1). However, this relative importance of *P* for self-expansion is highly variable across different regions and accounts for only 30% of the self-expansion in western Eurasia but up to 82% in Australia (fig. S13). Whereas self-expansion in the subtropics and the Southern Hemisphere drylands is primarily driven by reductions in upwind *P* contributions (fig. S13), increases in E_p are the major cause of self-expansion in the mid-latitude drylands of the Northern Hemisphere (fig. S14), which is consistent with the importance of *P* and

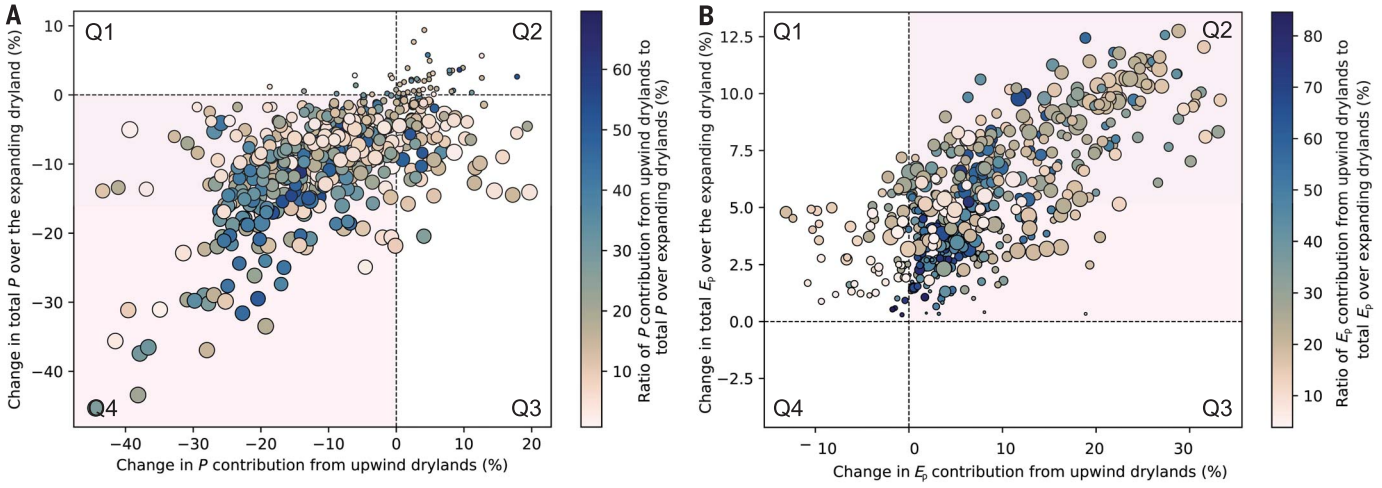

Fig. 2. Relative importance of changes in *P* and E_p contribution from upwind drylands in their expansion. (**A** and **B**) Relationship between percentage change in total (A) *P* or (B) E_p over expanding drylands (*y* axis) and the change in (A) *P* or (B) E_p contribution from upwind drylands to the expanding drylands (*x* axis). Each marker indicates a 1°-by-1° grid cell that has undergone a humid–dry transition and over which the Lagrangian model simulations are evaluated to estimate *P* and E_p contributions from upwind drylands. In total, the 540 grid cells represent ~5.2 million km^2 of transitioning land. The color of each marker indicates the mean contribution of upwind drylands to the total *P* and E_p in grid cells undergoing a humid–dry transition, calculated over the entire period of study (1981 to 2018). The size of the marker indicates the importance of changes in *P* and E_p to the increase in aridity over the drying humid regions; big markers indicate high importance, and small markers indicate low importance. Regions in quadrants (A) Q1 and Q2 and (B) Q3 and Q4 have undergone a humid–dry transition despite local net (A) increases in *P* or (B) decreases in E_p. Regions in quadrants (A) Q1 and (B) Q3 have undergone a net (A) increase in *P* or (B) decrease in E_p, respectively, despite a reduction in (A) *P* or an increase in (B) E_p contribution from upwind drylands. Regions in quadrants (A) Q3 and Q4 and (B) Q1 and Q2 have undergone a humid–dry transition because of a local (A) reduction in *P* or (B) an increase in E_p. Regions in (A) Q3 and (B) Q1 have witnessed (A) a reduction in *P* or (B) an increase in E_p despite (A) an increase in *P* or (B) a decrease in E_p contribution from upwind drylands—that is, no dryland self-expansion. Regions in (A) Q4 and (B) Q2 have experienced (A) a reduction in *P* or a (B) decrease in E_p partially because of (A) a reduction in *P* or (B) increase in E_p contribution from upwind drylands—that is, dryland self-expansion.

E_p changes for the observed increase in aridity in these regions.

Moisture and heat transport as a conduit of dryland self-expansion

In regions with a high climatological dependency on oceans and upwind humid lands for their supply of moisture (affecting *P*) and heat (affecting E_p), there is relatively low influence of dryland self-expansion. For example, the lower influence of self-expansion in regions such as East Africa can be attributed to the predominance of the ocean as a major source of moisture (*49*). Similarly, in regions where self-expansion plays a relatively small role such as the Caatinga, South America, and West Eurasia, a large proportion of the imported moisture and heat can be traced to the ocean and humid land areas (tables S2 and S3). In such regions, drylands have expanded into ~0.9 million km^2 of humid land despite an increase in *P* contribution or a decline in E_p contribution from upwind drylands—that is, without self-expansion (Fig. 2, Q3, and figs. S29 and S30). However, in some regions upwind drylands play a disproportional role in downwind aridification despite their importance as a source of moisture and heat to these regions being low. For example, in Australia 64.6% of the total increase in aridity is caused by self-expansion (Fig. 1), but climatologically, upwind drylands contribute only ~19% to total *P* and ~41% to total E_p on average (tables S2 and S3). Furthermore, in eastern Eurasia, for example, upwind drylands play an important role in dryland expansion (Fig. 1), even though humid regions form the primary source of both heat and moisture (tables S2 and S3). In most regions transitioning from humid to dryland, we found contributions to both declines in *P* and increases in E_p from existing upwind drylands (Fig. 2 and figs. S22 to S28). This raises the question: What causes the reduction in moisture and the increase in heat transport from upwind drylands into downwind humid regions that results in *P* deficits and E_p surpluses over them, and thus dryland self-expansion?

Upwind dryland aridification as a driving force of self-expansion

We hypothesize that changes in *P* and E_p over expanding drylands result mainly from the aridification of upwind drylands, which causes long-term changes in their land–atmosphere fluxes—that is, reduction in *E* and increase in *H*. Changes in surface fluxes can be initiated by various phenomena, including long-term circulation trends and climate oscillations. The methodological framework based on observationally constrained atmospheric transport modeling used in this study implicitly considers the impact of trends in circulation and the influence of climate oscillations on the modulation of upwind land fluxes and downwind heat and moisture transport. For example, the drying of the upwind drylands caused by more frequent blocking highs would still be considered as self-expansion if it translates into reduced *P* and increased E_p contribution from those upwind drylands to the downwind transitioning regions. To test our hypothesis, we grouped upwind drylands into two clusters —drying and wetting—on the basis of whether they have become more arid or humid during the period in which the downwind humid areas transitioned into drylands. Then, we compared the changes in upwind *P* and E_p contributions of both clusters (upwind drying and wetting drylands) with the AI of expanding drylands. Despite comparable areas of existing drylands undergoing drying (~29 million km^2) and wetting (~27 million km^2) (fig. S33), we found that the changes in *P* and E_p contributions to downwind aridification are an order of magnitude greater when upwind drylands experienced a drying trend (Fig. 3, C and D), which corroborates the importance of (upwind) dryland aridification for dryland self-expansion.

Although *P* contributions to AI from drying upwind drylands are largely negative (mean and spread of –16.1 ± 21.5 mm year^{-1} across all the expanding drylands), the *P* contributions

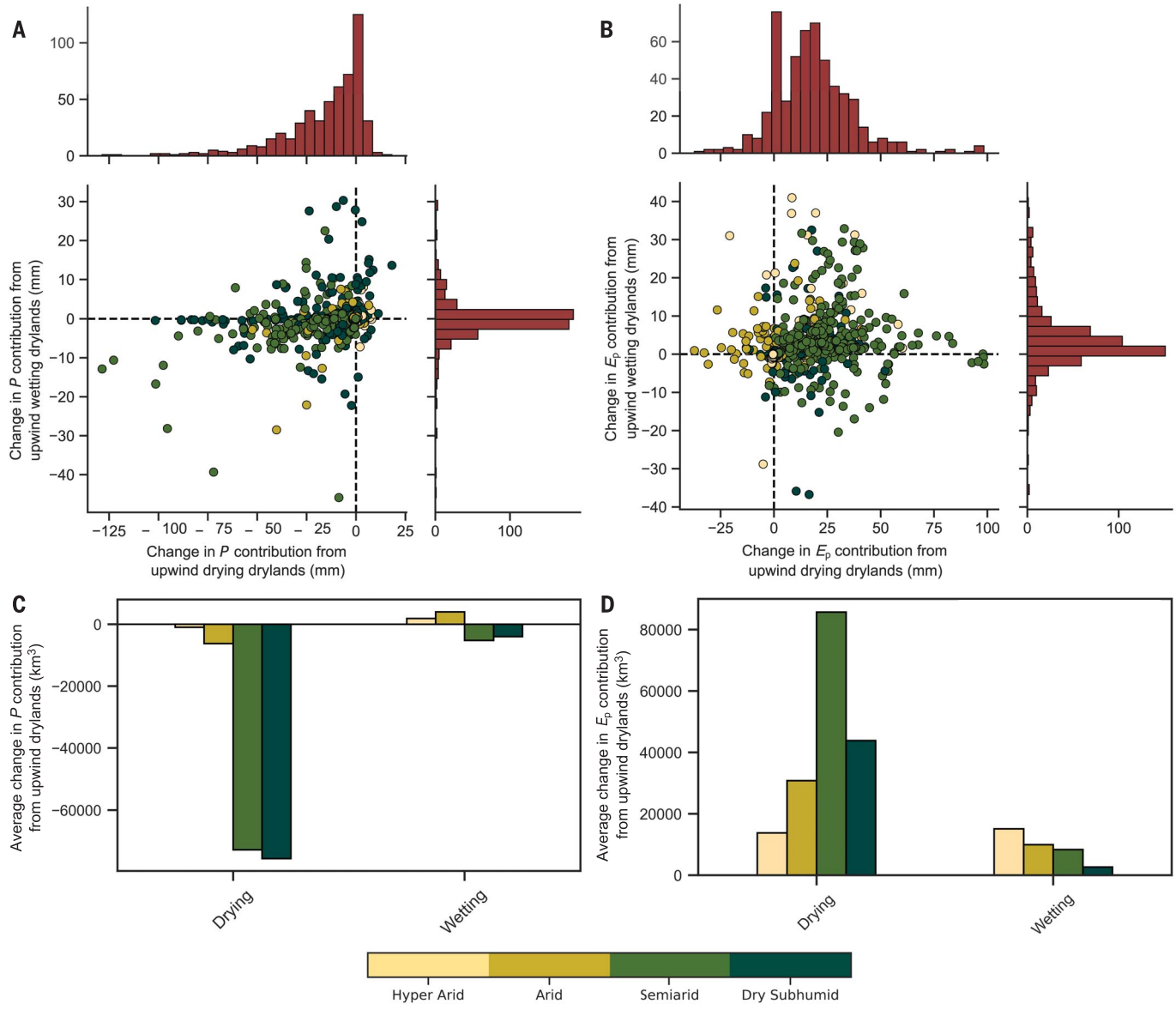

Fig. 3. Relative importance of drying and wetting upwind drylands for self-expansion. (**A** and **B**) Comparison of change in (A) *P* and (B) E_p contributions from upwind drylands, which are either drying (*x* axis) or wetting (*y* axis), to downwind regions that are undergoing a humid–dry transition. The color of each point indicates the aridity class (hyper arid, arid, semiarid, or dry subhumid) from which the maximum change in *P* or E_p contribution arises. (**C** and **D**) Bar plots show the average change in (C) *P* and (D) E_p contribution from drying and wetting upwind drylands [classified according to aridity classes detailed in (*23*)] to all the downwind regions undergoing a humid–dry transition; changes in *P* and E_p contributions from upwind drylands with different aridity classes have been averaged over all 540 grid cells, amounting to ~5.2 million km^2 of land area.

to AI changes from wetting drylands do not show substantial changes (–0.3 ± 6.0 mm year^{-1}). For example, the *P* contribution of the wetting western part of Australia (fig. S33) experienced an increase, whereas that of the drying eastern part experienced a decline (fig. S23). A similar conclusion can be drawn for the *P* contribution to dryland self-expansion from East Africa and southwestern United States, which have both had previously unrecorded levels of warming and aridification (*50*, *51*). Likewise, the change in E_p contributions to AI from drying drylands is positive (18.0 ± 18.7 mm year^{-1}). However, changes in E_p contributions from wetting drylands show a larger spread and less positive values (mean of 3.7 ± 8.5 mm year^{-1}). This is particularly evident in the increased sensible heat contribution from the Sahara, which has witnessed both drying and wetting (fig. S33), to dryland expansion not only in Africa but also in the eastern and western parts of Eurasia (figs. S22, S25, and S26).

Furthermore, a major proportion of the changes in *P* and E_p contributions globally can be attributed to semiarid and dry subhumid regions that have experienced a drying trend (Fig. 3). The large difference between the contributions of upwind drying and wetting drylands to self-expansion is due to the contrasting changes in land–atmosphere fluxes within them (fig. S34). We found that changes in both *E* (figs. S34, A to E) and *H* (fig. S34F) are substantially different between drying and wetting drylands, during the period in which downwind humid regions transitioned into a dryland. Although *H* has witnessed a

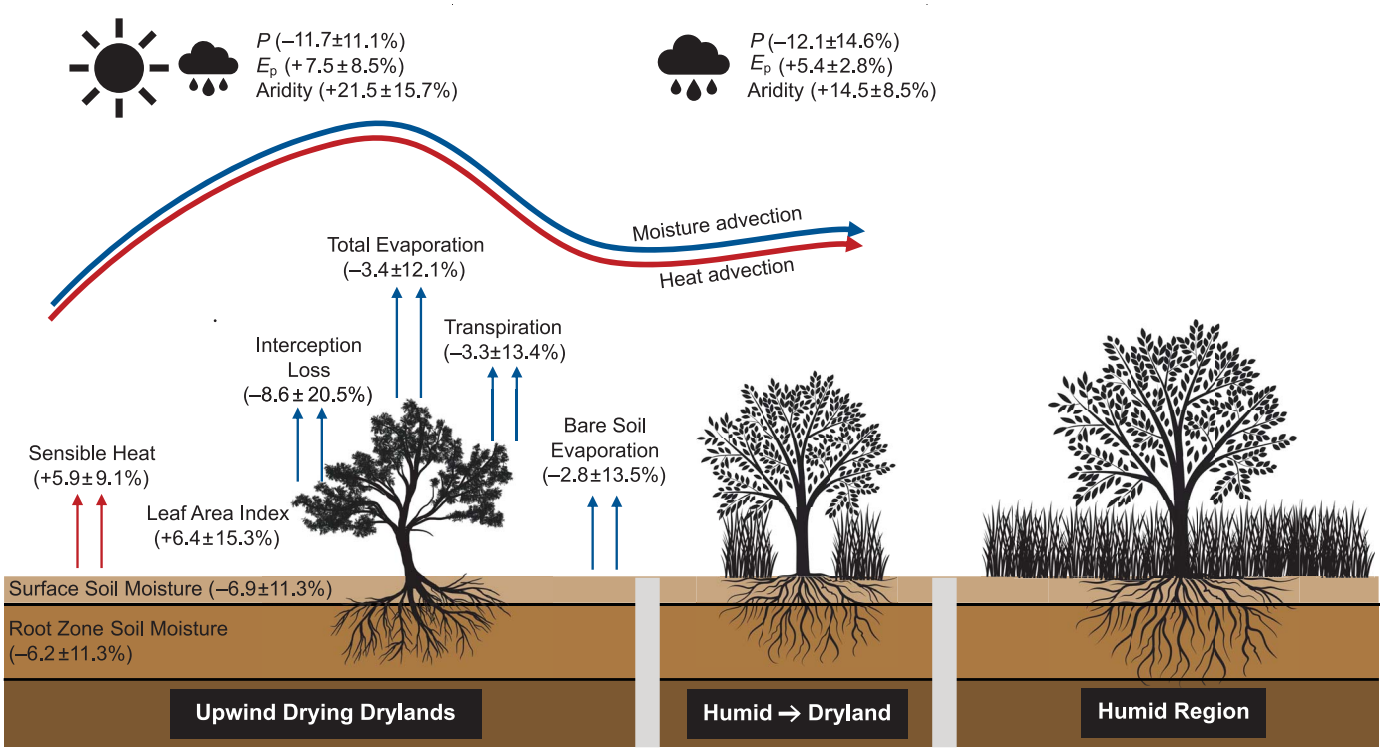

Fig. 4. Conceptual representation of the dryland expansion process. Aridification of upwind drylands due to both declines in *P* and increases in E_p leads to negative changes in soil water availability, which in turn results in changes in land–atmosphere fluxes. The reduced evaporation and increased sensible heating dries and warms the air in upwind drylands, which when advected downwind results in *P* declines and E_p surpluses over downwind humid regions and ultimately contributes to dryland expansion. The numbers are the global mean changes in various hydroclimatic variables in upwind drylands that are drying and the regions undergoing a humid–dry transition, estimated over the period 1981 to 2018. The average and spread (1 SD) of surface fluxes (sensible heat, total evaporation, interception loss, transpiration, and bare soil evaporation), LAI, and soil moisture (surface and root zone) over upwind drylands are weighted by the contribution of each upwind dryland grid cell to the changes in precipitation and potential evaporation over downwind regions undergoing a humid–dry transition (*23*).

nominal decline in wetting drylands (–0.5% ± 10.8%), it is substantially increased in their drying counterparts (5.9 ± 9.1%). Changes in *E* follow a similar pattern, with reductions in drying drylands (–3.4 ± 12.1%) and substantial increases in wetting drylands (12.3 ± 26.7%). L and E is increasingly unable to satisfy the increased atmospheric demand for water, with the ratio of *E* to E_p reduced by –6.1 ± 5.7% in drying drylands compared with a minor increase of 0.3 ± 6.9% in wetting drylands (fig. S34). The increased atmospheric water demand in upwind drylands is also a consequence of higher *H*. Therefore, changes in land–atmosphere fluxes and subsequent advection provide a mechanistic pathway for the downwind propagation of aridification.

Synthesis of the dryland self-expansion process and implications

Progressive aridification of existing drylands, initiated by global warming (*4*, *34*), is the primary trigger for dryland self-expansion (Fig. 4). Specifically, long-term decline in *P* and increase in E_p over drylands desiccate vegetation and soils, which in turn reduces evaporation. We found decreases in all components of evaporation, including transpiration, interception loss, and bare soil evaporation (Fig. 4). These declines occurred despite the greening of drylands seen in our results [leaf area index (LAI) increase of 6.4 ± 15.3% in drying and 18.8 ± 25.1% in wetting drylands, respectively] (figs. S35 and S36) and in previous assessments (*52*). Deficits in *E* are accompanied by an increase in *H*. These changes in both *E* and *H* are then propagated through the advection of drier and warmer air, respectively, to downwind humid regions, which results in deficits in *P* and surpluses in E_p. The persistence of this process over a sufficiently long period leads to expansion of drylands in the downwind direction. Thus, our results demonstrate the existence of a land–atmosphere feedback by which drylands may have spatially evolved historically and provide a theoretical framework for predicting their future expansion. With the projected increase in atmospheric aridity (*38*) and soil desiccation (*53*), coupled with potential saturation of vegetation greening (*14*), the dryland self-expansion mechanism elucidated here is expected to become more relevant in the future. Not only have we identified regions that are vulnerable to gradual and abrupt regime shifts, we also identified the upwind regions that are responsible for the aridification. By doing so, our results provide a scientific basis to help identify and design regionally targeted ecosystem management strategies in existing drylands to slow their rates of drying and consequent expansion.

REFERENCES AND NOTES

1. X. Lian *et al.*, *Nat. Rev. Earth Environ.* **2**, 232–250 (2021).
2. M. A. Asadi Zarch, B. Sivakumar, A. Sharma, *J. Hydrol. (Amst.)* **520**, 300–313 (2015).
3. D. S. Schimel, *Science* **327**, 418–419 (2010).
4. L. Wang *et al.*, *Nat. Clim. Chang.* **12**, 981–994 (2022).
5. A. Ahlström *et al.*, *Science* **348**, 895–899 (2015).
6. B. Poulter *et al.*, *Nature* **509**, 600–603 (2014).
7. C. Zhang, Y. Yang, D. Yang, X. Wu, *J. Hydrol.* **592**, 125618 (2021).
8. A. G. Koutroulis, *Sci. Total Environ.* **655**, 482–511 (2019).
9. J. Huang, H. Yu, X. Guan, G. Wang, R. Guo, *Nat. Clim. Chang.* **6**, 166–171 (2016).
10. S. I. Seneviratne *et al.*, *Earth Sci. Rev.* **99**, 125–161 (2010).
11. P. Greve *et al.*, *Nat. Geosci.* **7**, 716–721 (2014).
12. A. Berg, K. A. McColl, *Nat. Clim. Chang.* **11**, 331–337 (2021).
13. M. L. Roderick, P. Greve, G. D. Farquhar, *Water Resour. Res.* **51**, 5450–5463 (2015).
14. S. Wang *et al.*, *Science* **370**, 1295–1300 (2020).
15. F. Li *et al.*, *Science* **381**, 672–677 (2023).
16. J. G. Canadell *et al.*, in *Climate Change 2021 – The Physical Science Basis. Contribution of Working Group I to the Sixth Assessment Report of the Intergovernmental Panel on Climate Change*, V. Masson-Delmotte *et al.*, Eds. (Cambridge University Press, 2023), pp. 673–816.
17. S. I. Seneviratne *et al.*, in *Climate Change 2021 – The Physical Science Basis. Contribution of Working Group I to the Sixth Assessment Report of the Intergovernmental Panel on Climate*

Change, V. Masson-Delmotte *et al*., Eds. (Cambridge University Press, 2023), pp. 1513–1766.
18. Y. Yang *et al*., *Water Resour. Res.* **54**, 4700–4713 (2018).
19. J. T. Overpeck, B. Udall, *Proc. Natl. Acad. Sci. U.S.A.* **117**, 11856–11858 (2020).
20. P. C. D. Milly, K. A. Dunne, *Science* **367**, 1252–1255 (2020).
21. M. Berdugo *et al*., *Science* **367**, 787–790 (2020).
22. M. Delgado-Baquerizo *et al*., *Nature* **502**, 672–676 (2013).
23. Materials and methods are available as supplementary materials.
24. N. Middleton, D. S. G. Thomas, *World Atlas of Desertification* (Arnold, ed. 2, 1992).
25. J. L. Monteith, *Symp. Soc. Exp. Biol.* **19**, 205–234 (1965).
26. W. H. Maes, P. Gentine, N. E. C. Verhoest, D. G. Miralles, *Hydrol. Earth Syst. Sci.* **23**, 925–948 (2019).
27. C. M. Albano *et al*., *J. Hydrometeorol.* **23**, 505–519 (2022).
28. Z. Fang, W. Zhang, M. Brandt, A. M. Abdi, R. Fensholt, *Earths Futur.* **10**, e2022EF003019 (2022).
29. D. L. Ficklin, K. A. Novick, *J. Geophys. Res. Atmos.* **122**, 2061–2079 (2017).
30. D. Luo *et al*., *J. Geogr. Sci.* **33**, 449–463 (2023).
31. M. Alfaro-Córdoba, H. G. Hidalgo, E. J. Alfaro, *Atmosphere (Basel)* **11**, 427 (2020).
32. A. Mamalakis *et al*., *Nat. Clim. Chang.* **11**, 143–151 (2021).
33. T. G. Shepherd, *Nat. Geosci.* **7**, 703–708 (2014).
34. B. F. Zaitchik, M. Rodell, M. Biasutti, S. I. Seneviratne, *Nat. Water* **1**, 502–513 (2023).
35. P. J. Borah, V. Venugopal, J. Sukhatme, P. Muddebihal, B. N. Goswami, *Science* **370**, 1335–1338 (2020).
36. K. E. Trenberth *et al*., *Nat. Clim. Chang.* **4**, 17–22 (2014).
37. D. G. Miralles, P. Gentine, S. I. Seneviratne, A. J. Teuling, *Ann. N. Y. Acad. Sci.* **1436**, 19–35 (2019).
38. A. Berg *et al*., *Nat. Clim. Chang.* **6**, 869–874 (2016).
39. D. L. Schumacher, J. Keune, P. Dirmeyer, D. G. Miralles, *Nat. Geosci.* **15**, 262–268 (2022).
40. S. I. Seneviratne *et al*., *Geophys. Res. Lett.* **40**, 5212–5217 (2013).
41. D. L. Schumacher *et al*., *Nat. Geosci.* **12**, 712–717 (2019).
42. D. L. Schumacher, J. Keune, D. G. Miralles, *Ann. N. Y. Acad. Sci.* **1472**, 123–138 (2020).
43. D. R. Cayan *et al*., *Proc. Natl. Acad. Sci. U.S.A.* **107**, 21271–21276 (2010).
44. Y. Jiang *et al*., *Nat. Clim. Chang.* **9**, 617–622 (2019).
45. J. Jiang, T. Zhou, *Nat. Geosci.* **16**, 154–161 (2023).
46. F. Lopes Ribeiro *et al*., *Nat. Hazards Earth Syst. Sci.* **21**, 879–892 (2021).
47. T. J. Peterson, M. Saft, M. C. Peel, A. John, *Science* **372**, 745–749 (2021).
48. J. Keune, D. L. Schumacher, D. G. Miralles, *Geosci. Model Dev.* **15**, 1875–1898 (2022).
49. A. Koppa *et al*., *J. Geophys. Res. Atmos.* **128**, e2022JD038408 (2023).
50. J. E. Tierney, C. C. Ummenhofer, P. B. deMenocal, *Sci. Adv.* **1**, e1500682 (2015).
51. A. P. Williams *et al*., *Science* **368**, 314–318 (2020).
52. A. Gonsamo *et al*., *Glob. Change Biol.* **27**, 3336–3349 (2021).
53. L. Samaniego *et al*., *Nat. Clim. Chang.* **8**, 421–426 (2018).
54. F. F. Worku, M. Werner, N. Wright, P. Van Der Zaag, S. S. Demissie, *Hydrol. Earth Syst. Sci.* **18**, 3837–3853 (2014).
55. Z. Liu *et al*., *J. Geophys. Res. Atmos.* **125**, e2020JD032371 (2020).
56. A. Koppa, Data: Dryland self-expansion enabled by land-atmosphere feedbacks. Zenodo (2023); https://doi.org/10.5281/ZENODO.10408319.
57. J. Keune, A. Koppa, D. Miralles, FLEXPART–ERA-Interim simulations with 3 million parcels globally (1979–2019). Zenodo (2022); https://doi.org/10.5281/ZENODO.6947524.

ACKNOWLEDGMENTS

The computational resources and services used in this work were provided by the VSC (Flemish Supercomputer Center), funded by the Research Foundation, Flanders (FWO), and the Flemish Government. **Funding:** This study was funded by the European Union Horizon 2020 Programme (DOWN2EARTH, 869550). J.K. is grateful for the support from the Research Foundation Flanders (FWO) under grant 1244122N. D.G.M. acknowledges support from the European Research Council Consolidator grant, HEAT (101088405). D.L.S. and S.I.S. acknowledge partial funding support from the European Union's Horizon 2020 research and innovation program for the XAIDA project under grant agreement 101003469. **Author contributions:** A.K. and J.K. conceived the idea. A.K., J.K., and D.G.M. designed the experiments. J.K. conducted the global Lagrangian model simulations, with help from A.K.; A.K. performed the primary analysis of dryland self-expansion, with extensive inputs from J.K., D.G.M., and D.L.S.; A.K. drafted the first version of the manuscript, with substantial contributions from J.K. and D.G.M. All authors contributed to the interpretation of results and writing of the final version. **Competing interests:** The authors declare no competing interests. **Data and materials availability:** All outputs and code to reproduce the final figures are available at (*56*). The dataset of FLEXPART–ERA-Interim simulations containing 3 million parcels used for tracking heat and moisture in this study is available at (*57*).

SUPPLEMENTARY MATERIALS

science.org/doi/10.1126/science.adn6833
Materials and Methods
Supplementary Text
Figs. S1 to S36
Tables S1 to S3
References (*58*–*77*)

Submitted 21 December 2023; accepted 18 July 2024
10.1126/science.adn6833